Borrero-López, Antonio M.; Garcia Greca, Luiz; Rojas, Orlando J.; Tardy, Blaise L.

Controlling superstructure formation and macro-scale adhesion via confined evaporation of cellulose nanocrystals

Controlling superstructure formation and macro-scale adhesion via confined evaporation of cellulose nanocrystals

Antonio M. Borrero-López · Luiz G. Greca ·
Orlando J. Rojas · Blaise L. Tardy

Abstract The self-assembly of cellulose nanocrystals can tether their interfacial interactions and the associated properties of their constructs. For instance, assemblies of highly aligned cellulose nanocrystals (CNCs) bear improved mechanical strength, barrier properties, and piezoelectric response. In this study, the self-assembly of CNC superstructure was assessed under various confinement geometries, enabling optimization of the long-range order within the microstructures formed. The confinement involved the planar capillary (with a rectangular cross-section)formed between two glass substrates with silicone boundaries. The impact of temperature, width and thickness of the capillary plane on self-assembly of the micro-scaled lamellar structures was evaluated. Thinner capillaries and lower temperatures were found to considerably improve long-range order and increase the frequency of the periodic microstructures formed. The drying process was monitored by rheological analysis, which showed an initial fast drying followed by slow drying due to the hindered diffusion through lamellae. The adhesive properties of the formed superstructures were evaluated. The shear strength was shown to depend on the orientation of the superstructures and therefore of the CNCs. About 4 MPa adhesion strength was obtained when the lamellar superstructures were perpendicularly aligned with respect to the in-plane force applied, while *ca.* 3 MPa adhesion was obtained for parallel alignment. The experimental framework described herein enabled the evaluation of the impact of the dimensions of a drying meniscus on self-assembly of anisometric colloids while also linking cellulosic assemblies with their interfacial supramolecular interactions. This simple framework brings forward the possibility to correlate the behavior of nanometric objects with micro- and macro-scaled observations, *e.g.*, macro-scaled mechanics of adhesion.

A. M. Borrero-López · L. G. Greca · O. J. Rojas (✉) ·
B. L. Tardy (✉)
Department of Bioproducts and Biosystems, School of Chemical Engineering, Aalto University, P. O. Box 16300, FI-00076 Aalto, Espoo, Finland
e-mail: Orlando.rojas@ubc.ca

B. L. Tardy
e-mail: Blaise.tardy@ku.ac.ae

A. M. Borrero-López
Pro2TecS - Chemical Process and Product Technology Research Center, Departamento de Ingeniería Química, ETSI, Campus de "El Carmen", Universidad de Huelva, 21071 Huelva, Spain

O. J. Rojas
Bioproducts Institute, Department of Chemical and Biological Engineering, Department of Chemistry, Department of Wood Science, The University of British Columbia, Vancouver, BC V6T 1Z3, Canada

B. L. Tardy
Department of Chemical Engineering, Khalifa University, Abu Dhabi, United Arab Emirates

Introduction

The interfacial interactions and long-range order of
polysaccharides and other natural biopolymers have
numerous implications ranging from the fabrica-
tion of adhesives with a controlled end of life to the
formation of composites, including those obtained
via additive manufacturing (Yang et al. 2020; Li
et al. 2021a; Tardy et al. 2021). Of particular inter-
est, the nano-scaled supramolecular constructs of
cellulose, namely nanocelluloses, are key building
blocks towards the fabrication of sustainable materi-
als (Ajdary et al. 2020; Li et al. 2021b). Their aque-
ous processing has been widely studied, which has
resulted in a wide range of studies towards their
implementation as coatings, nanocomposites, porous
low-density constructs, etc. (Klockars et al. 2019;
Tardy et al. 2019; Yang et al. 2020). Controlling their
long-range order also enables the optimization of a
range of properties including piezoelectricity (Wang
et al. 2020), mechanical strength (Wang et al. 2017;
Mittal et al. 2018), optical properties (Parker et al.
2018; Wang et al. 2018; Kaschuk et al. 2022), barrier
properties (Chowdhury et al. 2019), or anisotropy of
mechanical response (Siqueira et al. 2017).

In a previous study, self-assembled CNC super-
structures were formed by evaporation induced self-
assembly between two glass substrates. The obtained
structures showed excellent adhesive properties, with
a dry strength comparable to commercial synthetic
adhesives (Tardy et al. 2020). The variables affecting
superstructure formation were broadly evaluated as a
function of atmospheric conditions. For instance, at
high humidity an increase in wetting resulted in an
increase in capillary forces between the two adhered
substrates and resulted in smaller and more frequent
microstructures formed (Tardy et al. 2020). Quantifi-
cation of the impact of assembly parameters was pre-
viously limited due to the lack of confinement of the
assembly configuration. For instance, previously, the
relationship between CNC contact area and adhesion
was elucidated. However, the impact of orientation

of CNCs was unclear. Isolation of the variables relat-
ing to superstructure formation was herein improved
by limiting the assembly to two drying edges instead
of four by applying silicon grease to two of the four
edges of the drying bond. This is reminiscent of sin-
gle capillary tube assembly, while bearing a higher
degree of freedom in designing the assembly config-
uration (Cherpak et al. 2018; Kim et al. 2021). There-
after, assembly and long-range order were evaluated
as a function of three different variables, namely,
volume assembled, distance between substrates, and
drying temperature (Fig. 1). Finally, we evaluate the
adhesion strength as a function of orientation of the
superstructures. Surprisingly, the supramolecular
interactions occurring from the cellulose chains pre-
sent on the colloids had a strong directional depend-
ence, which matched well to the directional anisot-
ropy of the coefficient of friction previously reported
at the nanoscale. The results provided herein show
that the interfacial interactions can be finely tuned
and scaled from the cellulose macromolecules up
to the cm-scale of the adhesive bonds. Additionally,
the variables explored herein such as temperature
and assembly configuration, offer another important
handle to tether superstructures formation and long-
range order of bio-colloidal assemblies.

Results and discussion

The main experimental methodology is described
in Fig. 1. Restricting the confined assembly resulted
in well-ordered micro-scaled, filament-like, lamel-
lae as can be seen across the manuscript. In the fol-
lowing experimental framework, the formation of
superstructured lamellae occurs by sequential frac-
tures of the consolidating CNC gel as a result of the
drying stresses (Tardy et al. 2020). The stresses are
a result of the capillary forces arising in the reced-
ing drying front. Inhomogeneity in concentration of
CNCs along the receding front result in a gradient of
stresses. Thereafter, the occurrence of fractures and
their pattern (*e.g.* spacing and width of the lamellae)
is directly proportional to these stress-fields that are a
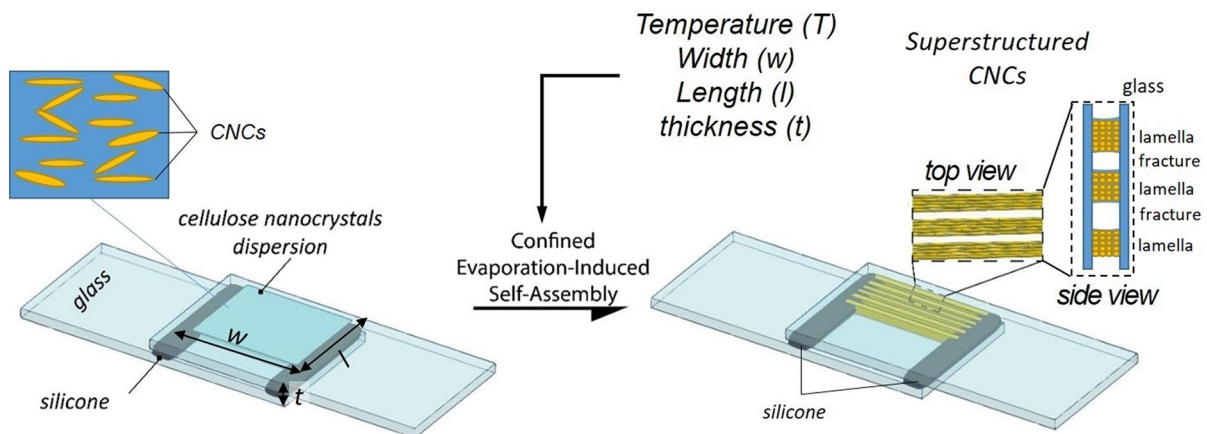function of concentration.

Fig. 1 Schematic of the drying configuration (left) and super-structures formed (right – as described in the magnified insets), wherein CNCs are aligned alongside microstructures (or lamellae) that formed perpendicularly to the drying front and containing aligned CNCs. The drying front is restricted to the area defined by the width "w" and thickness "t". Variables considered in this study, such as temperature and geometry of the assembly configuration, prior to confined evaporation induced self-assembly (C-EISA), are highlighted (temperature, width, length, thickness)

Impact of thickness on confined assembly

The first experimental framework evaluated the impact of the distance between substrates, which directly affects the thickness of lamellae. With decreasing thickness, capillary forces increase due to the increased Laplace pressure caused by a reduction in the radius of curvature of the meniscus at the drying front. The areal density was varied between 0.2 and 1 mg cm^{-2}, which refers to the amount of dry CNCs (from 5.5 wt% CNCs suspension) added with respect to the area initially covered by the suspension. Eight different thicknesses were studied (see Table S1) ranging from 37 to 174 μm to obtain trends on the impact of confinement in that range. As exemplified in the two micrographs included in Fig. 2a, thinner specimens resulted in higher initial contact area, corresponding to the area where lamellae are formed, and higher total amount of lamellae (Fig. 2b). The number of fractures increases exponentially with increased contact area, while it decreases exponentially with thickness (see Fig. 2b). The total number of fractures *vs.* the initial covered area and thickness were fitted using Eq. 1 and 2, respectively (see experimental section). Since initial covered area and thickness are related, the obtained parameters are interrelated. The parameters A and A_1 relate to the limits of the number of lamellae *vs.* initial covered area and thickness respectively. Meanwhile, the parameters t

and t_1 indicate the strength of the independent variable compared with the change in the number of lamellae. These parameters suggest a maximum number of lamellae, around 1450, when approaching contact (thickness of 0), which suggests an upper bound for the number of fractures. The good quality of the fits suggests that a higher alignment and a smoother concentration gradient are observed for thinner samples from their outer edge to the inner receding front, leading to more frequently occurring fractures within the nematically oriented gel intermediately formed. This is surprising as thicker samples would experience higher capillary flows, due to a higher evaporating area, and points to the fact that alignment occurs more pronouncedly for higher capillary pressures, as associated with the smaller meniscus of thinner samples.

Lamellae were not evenly distributed within the whole area. Generally, a higher concentration at the edges was found when compared with the center (Fig. 2c), which suggests that localized evaporation rate plays a significant role. Thicker samples had lower total fractures, and a lower density of fractures as well (Fig. 2c). Furthermore, a better alignment was also observed for thinner samples as indicated by a higher birefringence intensity when the samples are observed between polarizers. This indicates that fracture of the consolidating gel into microstructures also occurs as a function of the alignment—perpendicularly to
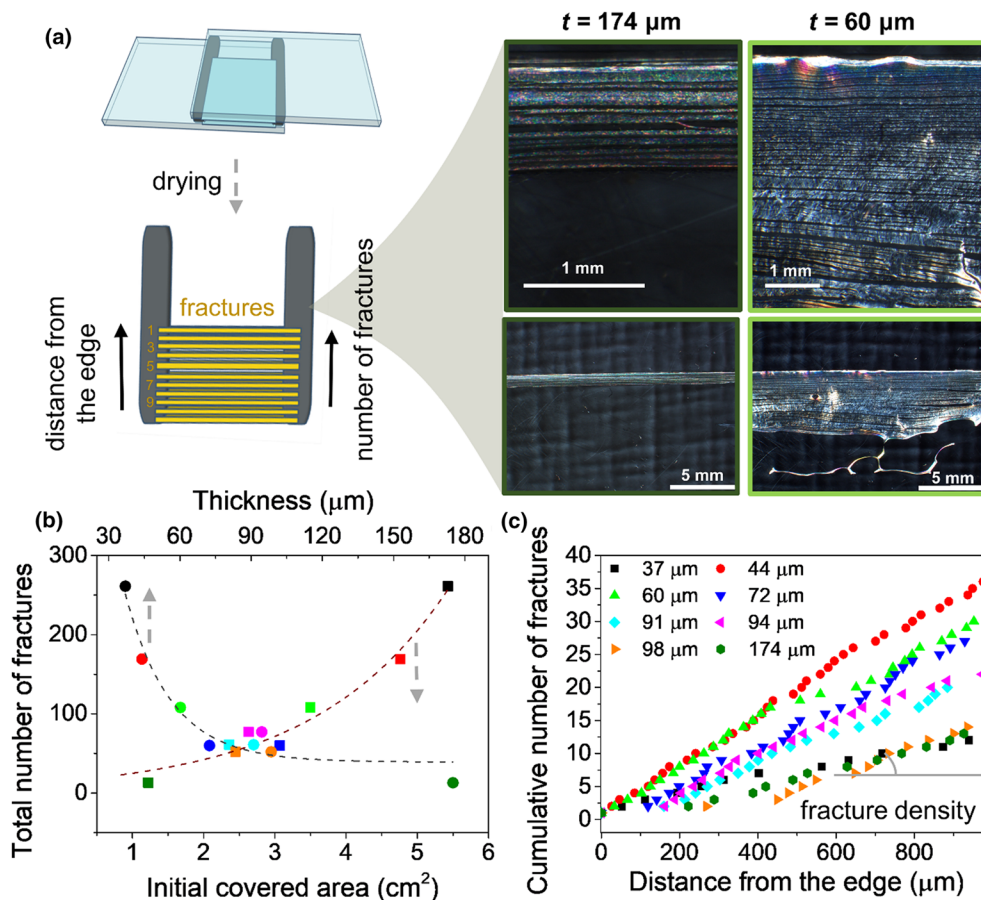
Fig. 2 a Schematic representation of the initial covered area (wet on top-left and dry at the bottom-left schematic) resulting from varying thickness (*t*) exemplified with two samples (right, thicknesses of 174 μm and 60 μm) as imaged between cross-polarizers where a higher intensity denotes a higher birefringence of the assembled layers. On the bottom-left scheme, lamellae are represented in yellow and fractures are the spaces between lamellae. Note that the silicone is not present in the imaged areas and would be visible on the left- and right-hand sides of the bottom micrographs. Lamellae have been numbered to illustrate the lamellae count. **b** Number of fractures according to both initial covered area and initial thickness. **c** Number of fractures *vs.* distance from the edge at different initial thicknesses

the drying front—as previously observed and associated with the path of least resistance (Tardy et al. 2020). Thereafter, the confined gel contracts towards its center point. In summary, higher alignment is expected to lead to more fractures, which are more closely spaced to each other's.

Further analysis of the corresponding histograms of the CNC lamellae width and inter-lamellae space distributions were also plotted, (Figs. S1 and S2, respectively). A general trend of narrower width and higher lamellar frequency with thinner specimens can be extrapolated (Fig. S3). This trend can also be more clearly observed by analyzing the modes (or maximas), as obtained from the

log-normal distributions, for both total quantity of lamellae and inter-lamellae distances as a function of thickness (Fig. S4). For inter-lamellae distances, the lamellae width was generally maintained, except for the thickest sample, which exhibited the largest mode for free spaces (Fig. S4).

Overall, thinner samples yielded smaller lamellae that were more closely spaced. For thicker samples, an increase in the disorder of the CNCs potentially prevented fracture generation and propagation, which would result in a larger contraction of the gels upon rupture. In conclusion, the generation and propagation of fractures was most pronouncedly related to alignment of the bio-colloids and secondarily to the
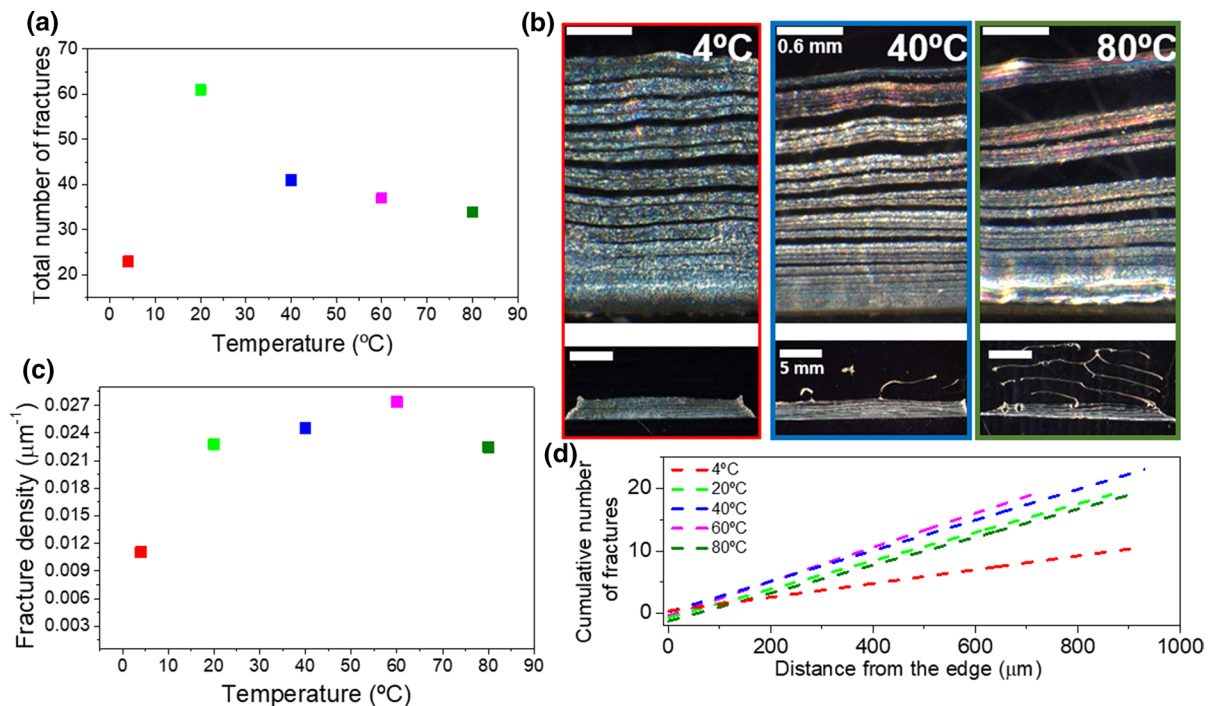
Fig. 3 a Number of fractures vs assembly temperature. **b** Micrographs obtained between cross-polarizers of specimens assembled at three different temperatures, with frames color coded respectively referring to the labels of (**a**). The upper image set is a magnification of the lower image set. **c** Fracture density at different temperatures. **d** Number of fractures in relation to the distance from the edge at different temperatures

concentration gradient present. Surprisingly, for thinner samples, this gradient seemed quite homogeneous as associated with the narrow dispersion of inter-lamellae distance (60 to 90% within 2–5 μm) and lamellae width (40% between 10 and 16 μm).

Impact of temperature on confined assembly

Temperature effect on the superstructure assembly was evaluated by applying different temperatures to specimens at an initial areal density of CNCs of ~0.5 mg cm^{-2}, within the temperature range of 4–80 °C. All the samples evaluated were included in Table S1, while some micrographs of the superstructures are displayed in Fig. 3b. In these images, it can be clearly observed that an increase in drying temperature led to a reduction in lamellae formation (Fig. 3a), where a maximum at room temperature was clearly noticeable. Large decreases were observed in the number of fractures when approaching the extreme temperatures (low and high), even more pronounced when the lowest temperature was considered. At high

temperature, reduced capillary forces (due to lower humidity and decreased surface tension) and higher drying rate prevented formation of a large contact area, while at low temperature slow self-assembly resulted in a more continuous layer instead of fractures being generated. A lower number of fractures is indicative of a homogeneous stress across the drying dispersion, which may indicate a more homogeneous dispersion concentration as associated with the slower evaporation at lower temperature. The latter is reminiscent of what was observed in circular capillary assembly (Cherpak et al. 2018). Nonetheless, even though the number of lamellae was lower for higher temperatures, a generally higher concentration of lamellae at the edges was observed (Fig. 3d), with higher birefringence colors (Fig. 3b). The different fractures densities allow an easier visualization, as exhibited in Fig. 3c.

The distribution of lamellae widths and spacings displayed similar characteristics as for the thickness study (Figs. S5–S7). Fig. S8 shows modes for both lamellae and spaces width, analyzing maximum percentage of occurrence at the mode as well. Not only a
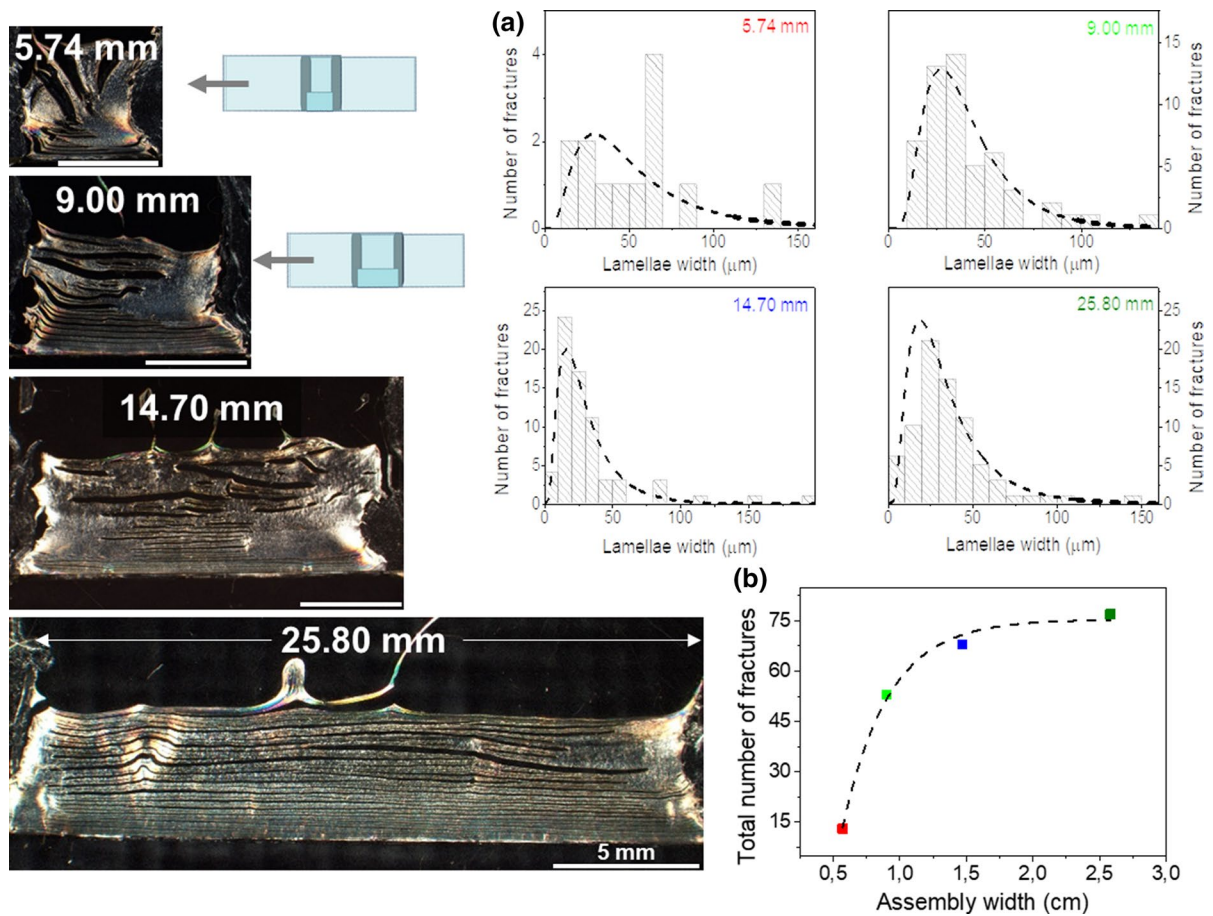
Fig. 4 Micrographs obtained between cross-polarizers of the lamellae superstructures obtained from the specimens with different initial widths. **a** Histograms of CNC lamellae widths as a function of specimen width. **b** The number of fractures in relation to the initial width

lower number of CNC lamellae but also a significantly higher width were observed at 4 °C-drying temperature, getting a mode more than three times higher than the remaining samples. On the other hand, maximum relative percentage and mode remained fairly constant for the remaining drying temperatures. Nonetheless, inter-lamellae spaces did show a clear trend, *i.e.*, the higher the temperature, the higher the concentration of very small spaces. This has been explained by the faster drying rate, which also supports the higher concentration of CNC lamellae found at the edges (see Fig. 3c).

Effect of edges distance on superstructure formation

The impact of the width of the assembly was finally evaluated to highlight the impact of the non-drying boundaries. Thereafter, the initial areal density of CNCs (*ca.* 0.5 mg cm^{-2}) and thickness (*ca.* 0.9 mm) were maintained. Four different specimen widths were tested, 5.74, 9.00, 14.70 and 25.80 mm (Table S1). Homogeneity of the formed superstructures was gradually lost by decreasing specimen widths, whereas lamellae alignment and extension were also seriously compromised, which suggests a width threshold in order to generate CNC lamellae for the whole covered area. The quantity of lamellae produced was dependent on specimen width (Fig. 4b), which suggests a soft threshold to minimize edge effects. 1.5 cm of width corresponds to the onset of such threshold, which will be dependent on temperature and thickness as well. This highlights that wider samples result in a more pronounced concentration

gradient or in a higher alignment of CNCs, where the latter can be associated with a larger drying front and thus higher evaporative convection (Klockars et al. 2019). Noticeably, narrower edges further correspond to previous work on capillary assembly, where fractures were not observed as well (Cherpak et al. 2018). Interestingly, this trend is opposite to the one observed when varying thickness, where samples with higher length/width ratio (lower thickness) corresponded to higher alignment and better-organized fractures, which points to a narrow range of thicknesses where fractures develop efficiently. A decreasing trend was observed in the number of fractures when reducing the width of assembly (see Fig. 4b and Eq. 3). The concentration of these lamellae was also very dependent on the distance to the edge, as can be seen in Fig. S9a. An exponential trend similar to that obtained for the number of fractures vs width specimen was shown, highlighting once more the importance of sufficient width to obtain fully-developed lamellae and proper drying (Fig. S9b).

Histograms from the developed samples with similar characteristics to those previously discussed were also analyzed for both lamellae and inter-lamellae spaces width (Fig. 4a & S10, respectively). In general, the smaller the specimen width, the broader the log-normal distribution of both fractures and inter-lamellae spaces (Fig. S11). The homogeneity usually observed gets seriously compromised when the narrowest sample is considered, as the outliers observed in histograms confirm (unusual significance of lamellae width around 6–7 and 13–14 microns). Narrower samples also exhibited higher values of the mode (around 27–29 microns against 16–18 microns for the widest ones). Besides, a higher relative percentage at the modes was also observed for the widest sample, *i.e.* around 74%, whereas only 28% was achieved for the narrowest one (see Fig. S12), highlighting the great homogeneity obtained at higher specimen width. Overall, a larger area for convection, *i.e.* a larger area at the drying front, enhances fracture occurrence and homogeneity.

The assembly configuration was also varied to non-rectangular geometries by tilting the sample (Figs. S13 and S14). Lamellae formation was enhanced by wider and thicker drying edges, showcasing flexibility in assembly configuration and resulting superstructure formation with the self-assembly strategy

described herein. The impact of gelation was also evaluated by rheological analysis.

Dynamics of lamellae consolidation

Viscoelastic functions, *i.e.*, storage and viscous moduli, can give insight on how elastic and viscous contributions impact a liquid system. This is especially interesting for colloidal suspensions and complex mixtures. Likewise, following their evolution through a determined process or with time is generally of a high interest. Therefore, the drying of the CNC suspension was monitored by time sweeps at different gaps and pre-shearing conditions to simulate the impact of drying on alignment. As shown in Fig. 5, in general, a pronounced increasing trend for both moduli was observed for the first 20–30 min, followed by an intermediate period where these moduli were kept fairly constant (30–300 min). In the case of larger gaps, the higher exposure to air led to faster drying, observed by the slightly higher values of both viscoelastic functions during the initial increasing trend. Afterwards, another small increase was noticed, finally reaching constant values during the remaining of the test (>1000 min). The first step may be governed by drying taking place at the edges, which is shown to be quite fast. Once the first lamellae are produced, they become a barrier for water losses from the sample, thus diffusion becomes the primary factor restricting drying and leading to the second regime. This fast toughening effect is explained by the fact that a higher number of fractures, with better alignment, are likely to be formed at the edges compared to the center of the geometry, due to the higher area of unhindered evaporation imposed by the setup. The final values are achieved once all water is released. It is worth mentioning that thickness did not demonstrate any effect as long as it was small enough to let lamellae be properly formed, while a fast pre-shearing led to a faintly small decrease in the final viscoelastic moduli. The latter observation suggests that the alignment induced by evaporation was more critical than that induced by pre-shearing.

Adhesion

The adhesion results showed that high shear strength can be obtained in both parallel and perpendicular directions in relation to the lamellae alignment

(Fig. 6), with the out-of-plane adhesion being considerably weaker due to the supramolecular nature of the interfacial interactions (Tardy et al. 2020). The data present a wide spread due to the brittle nature of the bond and the presence of defects, associated with imperfect alignment of the substrates. Of note, the upper boundaries are representative of the maximum adhesive strength as a function of orientation of the CNCs. Thereafter, the perpendicular out-of-plane adhesion was 73% higher than the parallel out-of-plane adhesion as a result of stress distribution being uneven in a bent sample (*i.e.* more load applied to the tip of the bond when considering the in-plane length). In contrast, in lap-shear the stresses were homogeneously applied yet resulted in 30% higher strength for the perpendicular samples. These values match surprisingly well, at the macro-scale, the anisotropy for coefficient of friction measured at the nano-scale for CNCs (Chae et al. 2020; Shishehbor et al. 2021). This further suggests that CNCs are well aligned and that this results in a high unidirectional alignment of the cellulose chain at the glass-cellulose chain interface.

Figure 6 relates to the correlation between orientation of the individual CNCs and orientation-dependent adhesive strength. Previously, contact area was shown to dominate the response of the adhesive rather than microstructure formation (lamellae and fractures as described herein) (Tardy et al. 2020). This was due to the brittle nature of the interface. To combine the findings put forward, on controlling fracture density and its influence on adhesive response, it would be desirable to form adhesives having a higher viscoelastic response. For instance, biomimetic adhesives, those reminiscent of what is observed in gecko feet or insects pads, have shown increased toughness when associated with smaller structures rather than larger ones, at an equivalent contact area (Kizilkan and Gorb, 2018).

Conclusions

The superstructures obtained by drying CNC aqueous dispersion in confined spaces demonstrate that the boundaries of evaporative confinement plays a crucial role in the formation of microstructures and the alignment of CNCs within lamellae. Drying temperature as well as thickness and width of the drying front define the superstructures' main characteristics, *i.e.* the width of lamellae and their periodicity. The thinner the specimen, the higher the density of the microstructures formed along the whole covered area, showing an exponential increase. An intermediate (ambient) temperature leads to the highest number of fractures, while severe reduction occurs for both lower and higher temperatures. At lower temperatures, a slower drying rate prevented the formation of fractures—possibly by reducing the internal stresses - while higher temperatures (and the associated faster drying rates) resulted in a loss of long-range order and thus a reduced tendency of the consolidating gel to fracture into microstructures. When evaluating different specimen widths, the widest samples exhibited a higher number of lamellae. In addition, homogeneity was partially lost by decreasing the width of the specimen, which suggests that an aspect-ratio threshold is required for full-length lamellae formation. The monitoring of viscoelastic functions allowed to further emphasize that the drying process is not homogeneous from the edges to the center of the bond. Therefore, a fast drying may form the first lamellae at the drying edge. Once those structures are formed, they become a barrier for water transfer, making diffusion more significant, and consequently slowing viscoelastic functions increase. The adhesion results evidenced that nano-scaled friction could be transferred into macro-scaled mechanics. When considering the main application explored so far for these superstructured CNCs, as adhesives, this would mean (1) a fine control over bond disruption, for instance, to replace the adhered part or, (2) as a fail-safe mechanism when load is applied in the wrong direction and the adhered part would otherwise break if strongly adhered. We expect that the framework proposed herein can be extended to a variety of bio-colloids and biopolymers, thus providing useful insights on long-range order under confinement as has been observed for large particles in composites (Mattos et al. 2020).

Materials and methods

Materials

Glass slides of $76 \times 26 \times 1$ mm^3 were obtained from VWR (Finland). CNCs (11.8%, w/v) were acquired

through the Process Development Center, University of Maine, USA. Produced by Forest Products Laboratory (FPL, Madison, WI) affiliated with United States Department of Agriculture. Except for rheological tests, a CNC solution diluted up to 5.5 wt% CNC content was used. Length and width 134 ± 52 nm and 7 ± 2 nm resp., sulfate half-ester content 335 mmol/kg, zeta potential *ca.* −47 mV (Reid et al. 2017). High viscosity silicone grease was used in all experiments. All chemicals were used as received.

Methods

Superstructure assembly

First of all, silicone grease was added onto the lower glass in order to delimit the drying front. Then, a determined amount (ranging within 6–25 mg) of CNC dispersion (5.5 wt% CNC) was added depending on the test. Finally, the top glass was placed onto the sample and gently pressed towards the lower glass to different extents, so that different thicknesses could be reached. Samples were generally dried at room temperature for several days. For high and low-temperature tests, samples were kept in the oven for *ca.* 2 h or in the fridge for *ca.* 1.5–2 days up to no presence of water and no changes in lamellae were observed. The covered area from the initial specimens along with CNC lamellae and inter-lamellae space width from dried samples were calculated by micrograph analysis with ImageJ processing software (version 1.8.0_112/1.52a).

Modelling of the total number of fractures obtained was accomplished by following different exponential equations, *i.e.*, Eq. 1 and 2 in the case of thickness study (according to the initial covered area and thickness respectively) and Eq. 3 in the case of width study (according to specimen width). Fits have been included in Figs. 2b and 4b.

$$CNC\,lamellae(thickness) = A \cdot e^{(initialcoveredarea/t)} \quad (1)$$

where A and t are the amplitude and decay constant parameters, whose values correspond to 14.81 and 1.9 cm^2.

$$CNC\,lamellae\,(thickness)$$
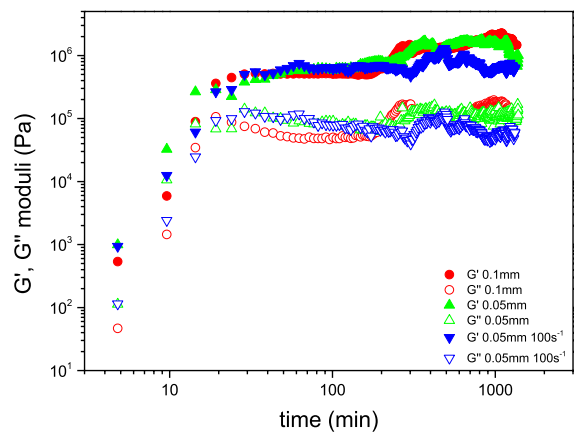$$= CNC\,lamellae_{\,t,final} - A_1 \cdot e^{(-thickness/t_1)} \quad (2)$$

Fig. 5 Viscoelastic moduli evolution as a function of drying time for 11.8 wt% CNC gels under different conditions including gap size (50 μm vs 100 μm, green and red labels respectively) and pre-shearing (blue labels)

A_1 and t_1 correspond to 1454 and 19.2 cm^2.

$$CNC\,lamellae\,(width) =$$
$$CNC\,lamellae_{w,final} - B \cdot e^{(-initialcoveredarea/z)} \quad (3)$$

where B and z had the same meaning as for Eq. 1, but values of 186 and 0.54 cm^2.

Optical microscopy

The optical micrographs were obtained in an Olympus SZX10 top-down microscope equipment. For a clear distinction between CNC lamellae and free spaces, some micrographs were obtained through a polarized film. Detailed information on the procedure can be found elsewhere (Tardy et al. 2020). Further analysis of the corresponding histograms of the CNC lamellae width and inter-lamellae spaces distributions was performed with a constant bin of 10 μm for all of the specimens.

Rheological tests

Dynamic time sweeps were performed by applying a determined constant stress within the linear range, previously calculated through strain sweeps, for 22 h. For this study, 11 wt% CNC dispersion, which becomes a gel, was used, as an adequate stress within the linear viscoelastic range is more feasible to be obtained along the whole experiment using 25 mm
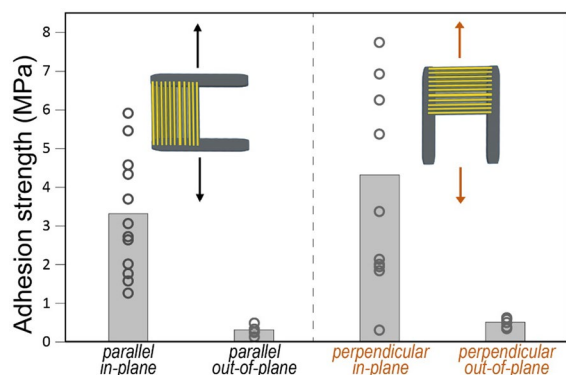
Fig. 6 Adhesion strength as a function of orientation of super-structures and loading direction

diameter plate-plate geometry. Different gaps (0.05, 0.1 and 1 mm) and pre-shearing (1 or 100 s^{-1} applied for several minutes) were evaluated. The equipment used was a MCR 302 (Anton Paar, Austria).

Adhesion test

The in-plane and out-of-plane adhesion tests were performed in a MTS 400 M tensile tester by applying a strain rate of 1.5 mm/min and using a 2 kN load cell. For the in-plane tests, the gauge length was kept at *ca.* 60 mm. For the out-of-plane, the samples were fixed in the horizontal plane and pushed (with the MTS 400 M operating under compression mode) at a point closest to the edge of the overlapping glass substrates. Of note, control samples were tested for in- and out-of-plane adhesion with the silicone grease alone. The obtained in-plane adhesion strengths in-plane were negligible and in the out-of-plane case were at most lower than 10% of the average.

Declarations

References

Ajdary R, Tardy BL, Mattos BD et al (2020) Plant nanomaterials and inspiration from nature: water interactions and hierarchically structured hydrogels. Adv Mater 33:2001085. https://doi.org/10.1002/adma.202001085

Chae I, Ngo D, Chen Z et al (2020) Anisotropic optical and frictional properties of Langmuir-Blodgett film consisting of uniaxially-aligned rod-shaped cellulose nanocrystals. Adv Mater Interfaces 7:1902169. https://doi.org/10.1002/admi.201902169

Cherpak V, Korolovych VF, Geryak R et al (2018) Robust chiral organization of cellulose nanocrystals in capillary confinement. Nano Lett 18:6770–6777. https://doi.org/10.1021/acs.nanolett.8b02522

Chowdhury RA, Nuruddin M, Clarkson C et al (2019) Cellulose nanocrystal (CNC) coatings with controlled anisotropy as high-performance gas barrier films. ACS Appl Mater Interfaces 11:1376–1383. https://doi.org/10.1021/acsami.8b16897

Kaschuk JJ, Al Haj Y, Rojas OJ et al (2022) Plant-based structures as an opportunity to engineer optical functions in next-generation light management. Adv Mater 34:2104473. https://doi.org/10.1002/adma.202104473

Kim M, Pierce K, Krecker M et al (2021) Monolithic chiral nematic organization of cellulose nanocrystals under capillary confinement. ACS Nano 15:19418–19429. https://doi.org/10.1021/acsnano.1c05988

Kizilkan E, Gorb SN (2018) Combined effect of the microstructure and underlying surface curvature on the performance of biomimetic adhesives. Adv Mater 30:1704696. https://doi.org/10.1002/adma.201704696

Klockars KW, Yau NE, Tardy BL et al (2019) Asymmetrical coffee rings from cellulose nanocrystals and prospects in art and design. Cellulose 26:491–506. https://doi.org/10.1007/s10570-018-2167-7

Li K, Clarkson CM, Wang L et al (2021a) Alignment of cellulose nanofibers: harnessing nanoscale properties to macroscale benefits. ACS Nano 15:3646–3673. https://doi.org/10.1021/acsnano.0c07613

Li T, Chen C, Brozena AH et al (2021b) Developing fibrillated cellulose as a sustainable technological material. Nature 590:47–56. https://doi.org/10.1038/s41586-020-03167-7

Mattos BD, Tardy BL, Greca LG et al (2020) Nanofibrillar networks enable universal assembly of superstructured particle constructs. Sci Adv 6:eaaz7328. https://doi.org/10.1126/sciadv.aaz7328

Mittal N, Ansari F, Gowda Krishne V et al (2018) Multiscale control of nanocellulose assembly: transferring remarkable nanoscale fibril mechanics to macroscale fibers. ACS Nano 12:6378–6388. https://doi.org/10.1021/acsnano.8b01084

Parker RM, Guidetti G, Williams CA et al (2018) The self-assembly of cellulose nanocrystals: hierarchical design of visual appearance. Adv Mater 30:1704477. https://doi.org/10.1002/adma.201704477

Reid MS, Villalobos M, Cranston ED (2017) Benchmarking cellulose nanocrystals: from the laboratory to industrial production. Langmuir 33:1583–1598. https://doi.org/10.1021/acs.langmuir.6b03765

Shishehbor M, Son H, Nuruddin M et al (2021) Influence of alignment and microstructure features on the mechanical properties and failure mechanisms of cellulose nanocrystals (CNC) films. J Mech Behav Biomed Mater 118:104399. https://doi.org/10.1016/j.jmbbm.2021.104399

Siqueira G, Kokkinis D, Libanori R et al (2017) Cellulose nanocrystal inks for 3D printing of textured cellular architectures. Adv Funct Mater 27:1604619. https://doi.org/10.1002/adfm.201604619

Tardy BL, Mattos BD, Greca LG et al (2019) Biomimetic templating: tessellation of chiral-nematic cellulose nanocrystal films by microtemplating (Adv. Funct. Mater. 25/2019). Adv Funct Mater 29:1970169. https://doi.org/10.1002/adfm.201970169

Tardy BL, Richardson JJ, Greca LG et al (2020) Exploiting supramolecular interactions from polymeric colloids for strong anisotropic adhesion between solid surfaces. Adv Mater 32:1906886. https://doi.org/10.1002/adma.201906886

Tardy BL, Mattos BD, Otoni CG et al (2021) Deconstruction and reassembly of renewable polymers and biocolloids into next generation structured materials. Chem Rev 121:14088–14188. https://doi.org/10.1021/acs.chemrev.0c01333

Wang J, Carlos C, Zhang Z et al (2020) Piezoelectric nanocellulose thin film with large-scale vertical crystal alignment. ACS Appl Mater Interfaces 12:26399–26404. https://doi.org/10.1021/acsami.0c05680

Wang S, Jiang F, Xu X et al (2017) Super-strong, super-stiff macrofibers with aligned, long bacterial cellulose nanofibers. Adv Mater 29:1702498. https://doi.org/10.1002/adma.201702498

Wang S, Li T, Chen C et al (2018) Transparent, anisotropic biofilm with aligned bacterial cellulose nanofibers. Adv Funct Mater 28:1707491. https://doi.org/10.1002/adfm.201707491

Yang X, Biswas SK, Han J et al (2020) Surface and interface engineering for nanocellulosic advanced materials. Adv Mater 33:2002264. https://doi.org/10.1002/adma.202002264